COMPRESSED SENSING FOR DOSE REDUCTION IN STEM TOMOGRAPHY

*L. Donati, M. Nilchian, M. Unser**

Biomedical Imaging Group,
EPFL, Lausanne, Switzerland

S. Trépout, C. Messaoudi, S. Marco†

Inserm U1196,
Institut Curie, Orsay, France

ABSTRACT

We designed a complete acquisition-reconstruction framework to reduce the radiation dosage in 3D scanning transmission electron microscopy (STEM). Projection measurements are acquired by randomly scanning a subset of pixels at every tilt-view (*i.e.*, random-beam STEM or "RB-STEM"). High-quality images are then recovered from the randomly downsampled measurements through a regularized tomographic reconstruction framework. By fulfilling the compressed sensing requirements, the proposed approach improves the reconstruction of heavily-downsampled RB-STEM measurements over the current state-of-the-art technique. This development opens new perspectives in the search for methods permitting lower-dose 3D STEM imaging of electron-sensitive samples without degrading the quality of the reconstructed volume. A Matlab code implementing the proposed reconstruction algorithm has been made available online.

Index Terms— STEM tomography, dose reduction, compressed sensing, random-beam scanning, regularized reconstruction.

1. INTRODUCTION

Scanning transmission electron microscopy (STEM) is a powerful imaging method that permits visualization of biological structures at the nanoscale [1]. In 3D STEM, a focused electron beam scans the sample in a raster and the transmitted radiation is detected. The sample is rotated over a range of tilt angles and projection images from multiple directions are collected (Figure 1a-b). A volume is then computationally reconstructed from the set of projection measurements.

STEM offers several advantages over conventional electron tomography, such as a better signal-to-noise ratio (SNR) and enhanced contrast [2, 3, 4]. Yet, it suffers from the same experimental limitation: high-resolution imaging requires large electron radiation dosage, to which most biological specimens are extremely sensitive. A trade-off between the reconstruction quality and the sample integrity is thus *de rigueur* when optimizing 3D STEM imaging. Various methods have been developed to permit lower-dose 3D STEM acquisition without degrading the quality of the reconstructed volume. These techniques can be categorized according to whether the dosage reduction is achieved by angular downsampling or spatial downsampling [5].

Tilt-downsampling (T-DS) approaches rely on algorithms that reconstruct a tomographic image from a reduced number of angular views (Figure 1c) [6, 7, 8, 9, 10, 11]. By contrast, image-downsampling (I-DS) techniques aim to reduce the electron coverage of individual tilt images. One way to achieve this is by decreasing the per-pixel dwell time or the beam current density [12]. Alternatively, one can scan only a fraction of the pixels following a certain downsampling pattern, *e.g.* uniform or random (Figure 1d-e) [13, 14].

The recovery of randomly-downsampled STEM images has been the pioneered work of a recent publication by Saghi *et al* [5]. The authors proposed to perform the reconstruction in two steps. They first filled in the missing data through TV-inpainting in order to produce conventional projections. They then used an iterative algorithm with TV-regularization for the tomographic reconstruction of the projection views. By doing so, they could demonstrate the feasibility of further reducing the electron dosage in STEM through the random scanning of a subset of pixels. Yet, as we shall later argue, their reconstruction algorithm does not take advantage of the theory of compressed sensing (CS), which predicts that sparse signals can be acquired with a minimum number of measurements provided that proper recovery methods are used [15]. Therefore, although CS may provide an ideal framework for minimizing the electron dosage in tomographic STEM imaging, its potential in this regard has not been entirely exploited yet.

To address this gap, we have designed an acquisition-reconstruction framework named random-beam STEM (or "RB-STEM") which take advantage of the principles of CS to tomographic STEM. We present here the regularized tomographic reconstruction framework we have designed to reconstruct high-quality images from incoherent RB-STEM datasets. We demonstrate through simulations that the pro-

*The work of Laurène Donati and Masih Nilchian was funded by an ERC grant (ERC-692726-GlobalBioIm).

†The work of Sylvain Trépout and Cédric Messaoudi was funded by an ANR grant (ANR-11-BSV8-016).

978-1-5090-1172-8/17/$31.00 ©2017 IEEE

posed algorithm has the potential to achieve superior reconstructions of highly detailed objects imaged at low electron dose.

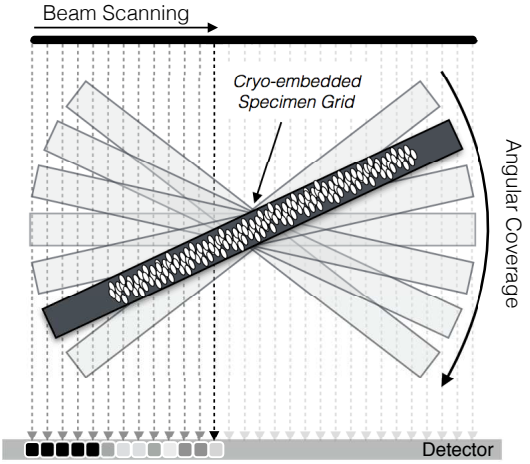

(a) Conventional 3D cryo-STEM set-up

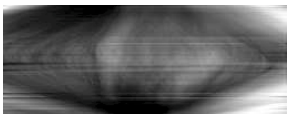

(b) Full Tomogram (no DS)

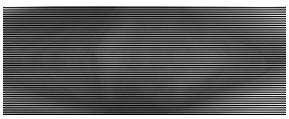

(c) Uniform T-DS (50%)

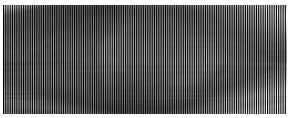

(d) Uniform I-DS (50%)

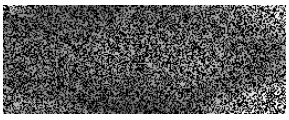

(e) Random I-DS (50%)

Fig. 1. Dose reduction approaches in cryo-STEM. (**a**) Illustration of a conventional cryo-STEM set-up. (**b**) Full tomogram (horizontal-axis: projection plane coordinates, vertical-axis: tilt-angles). (**c**)-(**e**) Effect on tomogram of the considered downsampling approaches (shown here with a 50% DS ratio). *DS*: downsampling, *T-DS*: tilt-downsampling, *I-DS*: image-downsampling.

2. RB-STEM: ACQUISITION

RB-STEM consists in the random scanning of a subset of pixels for every tilt view (Figure 1e). Similarly to conventional STEM, the scanning process in RB-STEM mode corresponds to the straight-line transmission of an electron beam through the sample. It can be thus mathematically described through the X-ray transform $\mathcal{P} : L_2\left(\mathbb{R}^3\right) \rightarrow L_2(\mathbb{R}^2 \times [0, \pi))$, which maps a 3D function $f(\boldsymbol{x})$ into its 2D line-integral images along different tilt angles, *i.e.*:

$$\mathcal{P}\{f(\boldsymbol{x})\}(\boldsymbol{y}; \theta) = \int_{\mathbb{R}^3} f(\boldsymbol{x})\delta(y_1 - x_1 \cos\theta - x_2 \sin\theta, y_2 - x_3)\mathrm{d}\boldsymbol{x}\,. \quad (1)$$

Here $\theta \in [0, \pi)$, while $\boldsymbol{x} = (x_1, x_2, x_3)$ and $\boldsymbol{y} = (y_1, y_2)$ specify the object and projection coordinates, respectively. The $\delta(\mathbf{x})$ denotes the two-dimensional delta function.

3. RB-STEM: RECONSTRUCTION

The task is to reconstruct a three-dimensional signal f from a set of RB-STEM measurements $g(\boldsymbol{y}_i, \theta_i)$, with $(\boldsymbol{y}_i, \theta_i) \in Y \times \Theta$. Here $i \in \{1, 2, \cdots, M\}$, where M corresponds to the number of projection measurements. The set Y contains the different positions of the STEM gun scans on the projection plane. The set of all tilt angles is collected in Θ.

3.1. Discretization Scheme

We first need to discretize the signal and the imaging operator in order to formulate the reconstruction as an inverse problem. The standard approach consists in fixing the reconstruction space to functions of the form [16, 17]:

$$f(\boldsymbol{x}) = \sum_{\boldsymbol{k} \in \Omega} c_{\boldsymbol{k}} \varphi(\boldsymbol{x} - \boldsymbol{k})\,. \quad (2)$$

The function $f(\boldsymbol{x})$ is then described by its coefficients $c_{\boldsymbol{k}}$. The $\varphi(\cdot - \mathbf{k}) \in L_2(\mathbb{R}^3)$ with $\boldsymbol{k} = (k_1, k_2, k_3) \in \mathbb{Z}^3$ are appropriate functions, while $\Omega = \{-N_1 \cdots N_1\} \times \{-N_2 \cdots N_2\} \times \{-N_3 \cdots N_3\}$ specifies the support of the object $(N_1, N_2, N_3 \in \mathbb{N})$. By the linearity and the pseudo-shift-invariance of the X-ray transform [18], we then model the effect of the projection operator $\mathcal{P}$ by:

$$\mathcal{P}f(\boldsymbol{y}; \theta) = g(\boldsymbol{y}; \theta) = \sum_{\boldsymbol{k} \in \Omega} c_{\boldsymbol{k}} \mathcal{P}\varphi(y_1 - k_1 \cos\theta - k_2 \sin\theta, y_2 - k_3; \theta)\,. \quad (3)$$

We then write the STEM imaging model in matrix form as:

$$\mathbf{g} = \mathbf{H}\,\mathbf{c}\,. \quad (4)$$

Here, $\mathbf{g} \in \mathbb{R}^M$ with entries $[\mathbf{g}]_i = g(\boldsymbol{y}_i, \theta_i)$, while $\mathbf{c} \in \mathbb{R}^N$ is a vector representation of the coefficients (Eq. (2)) indexed by $\mathbf{k}$ with $N = (2N_1 + 1)(2N_2 + 1)(2N_3 + 1)$. The entries of the system matrix $\mathbf{H} \in \mathbb{R}^{M \times N}$ are $[\mathbf{H}]_{i,\boldsymbol{k}} = \mathcal{P}\varphi(y_{i,1} - k_1 \cos\theta_i - k_2 \sin\theta_i, y_{i,2} - k_3; \theta_i)$, where $[\boldsymbol{y}]_i = (y_{i,1}, y_{i,2})$.

In RB-STEM, the acquired measurements positions $(\boldsymbol{y}_i, \theta_i)$ are predetermined by a random sub-scanning pattern S. We can thus denote the set of positions by $(\boldsymbol{y}_i, \theta_i) \in Y_S \times \Theta_S$ where the elements in the set $Y_S \times \Theta_S$ are specified by the sampling pattern S.

3.2. Reconstruction Algorithm

The task of reconstructing heavily downsampled RB-STEM measurements is a strongly ill-posed inverse problem. Nevertheless, the theory of compressed sensing asserts that under appropriate conditions, one can solve this problem through l_1-minimization [15]. The matrix formulation is as follows:

$$\min_{\mathbf{c}\in\mathbf{R}^n} \|\mathbf{L}\,\mathbf{c}\|_1 \text{ subject to } \|\,\mathbf{H}\,\mathbf{c}-\mathbf{g}\|^2 \leq \epsilon\,, \tag{5}$$

where $\mathbf{L}$ specifies the sparsifying operator that transforms the signal. The equivalent Lagrange formulation of the optimization is:

$$\mathcal{J}(\mathbf{c}) = \min_{\mathbf{c}\in\mathbf{R}^n} \left\{ \frac{1}{2}\|\,\mathbf{H}\,\mathbf{c}-\mathbf{g}\|^2 + \lambda\|\mathbf{L}\,\mathbf{c}\|_1 \right\}. \tag{6}$$

We define the auxiliary variable $\mathbf{u} = \mathbf{L}\,\mathbf{c}$ and rewrite the optimization problem as a constrained optimization problem [19, 20]. The scaled augmented Lagrangian functional is then given by:

$$\mathcal{L}_\mu(\mathbf{c},\mathbf{u},\mathbf{d}) = \frac{1}{2}\|\,\mathbf{H}\,\mathbf{c}-\mathbf{g}\|^2 + \lambda\|\mathbf{u}\|_1 + \frac{\mu}{2}\|\mathbf{u}-\mathbf{L}\,\mathbf{c}+\mathbf{d}\|^2\,. \tag{7}$$

where $\mathbf{d}$ is the Lagrange variable. This optimization problem is decomposed into a set of simpler ones by using the alternating direction method of multipliers (ADMM) [19, 20]:

$$\begin{cases} \mathbf{c}^{k+1} \leftarrow \underset{\mathbf{c}}{\operatorname{argmin}}\ \mathcal{L}_\mu(\mathbf{c},\mathbf{u}^k,\mathbf{d}^k) & (a) \\ \mathbf{u}^{k+1} \leftarrow \underset{\mathbf{u}}{\operatorname{argmin}}\ \mathcal{L}_\mu(\mathbf{c}^{k+1},\mathbf{u},\mathbf{d}^k) & (b) \\ \mathbf{d}^{k+1} \leftarrow \mathbf{d}^k + \mu(\mathbf{L}\mathbf{c}^{k+1}-\mathbf{u}^{k+1}) & (c) \end{cases} \tag{8}$$

Eq. 8(a) is a quadratic minimization with respect to $\mathbf{c}$. The critical point of the cost functional is the root of its gradient function, *i.e.*:

$$\mathbf{c} = \left(\mathbf{H}^\top\mathbf{H} + \mu\mathbf{L}^\top\mathbf{L}\right)^{-1}\left(\mathbf{H}^\top\mathbf{g} + \mu\mathbf{L}^\top(\mathbf{u}+\mathbf{d})\right). \tag{9}$$

Since the matrix $\left(\mathbf{H}^\top\mathbf{H} + \mu\mathbf{L}^\top\mathbf{L}\right)$ is not directly invertible, we use a conjugate gradient algorithm to minimize Eq. 8(a).

The solution of Eq. 8(b) is a simple point-wise soft-thresholding operator,

$$\mathbf{u}^{k+1} = \operatorname{prox}_{\frac{\lambda}{\mu}}(\mathbf{L}\mathbf{c}^{k+1}-\mathbf{d}^k)\,. \tag{10}$$

Finally, the last step (Eq. 8(c)) corresponds to an update of the Lagrange parameter.

4. EXPERIMENTS

We compared our integrated framework for the reconstruction of randomly-downsampled STEM measurements to the prior approach proposed in [5].

4.1. Simulation Conditions

Experiments were performed using a $512\times512\times256$ ground-truth volume depicting the flagellar pocket of a trypanosome (Figure 2a). All simulations were implemented in Matlab (MathWorks, Natick, MA, USA). Two variants of the projection operator were coded to simulate the acquisition process: one using Kaiser-Bessel window functions (KBWF) as discretizing functions and one based on B-splines [21]. This permits the selection of distinct operators for the acquisition and reconstruction tasks, hence reducing the risk of committing an "inverse crime".

To mimic the "missing cone of information" effect, we considered an angular coverage of $(-70°;+70°)$, with an angular increment of $1°$. Random image-downsampling (I-DS) was achieved by applying a subsampled binary mask over the simulated projection measurements. The considered randomized regime followed an uniform distribution.

Our reconstruction framework was implemented as described in *Section 3.2*. Isotropic total-variation (TV) regularization was used to promote sparsity. The pioneer algorithm was reimplemented as described in [5]. The optimization of the hyper-parameters was performed by visual assessment.

4.2. Reconstruction Results

Figure 2b-e presents xy-orthoslices views of the reconstructions of RB-STEM data achieved by both frameworks at 50% and 20% downsampling ratios. The corresponding Fourier shell correlation (FSC) are displayed in Figure 2f. Visual and quantitative analysis of these results indicate that, at equivalent dose reduction, the proposed RB-STEM reconstruction algorithm significantly outperforms the state-of-the-art algorithm. Finer details (*e.g.*, filament-like structures) can be visually retrieved from the reconstructions achieved by our framework, at both 50% and 20% downsampling. In addition, the FSC curves indicate that the proposed algorithm achieves significantly higher resolution at both sampling levels. Two main reasons might be put forward to explain those improvements.

First, the proposed RB-STEM algorithm performs the tomographic reconstruction in a single, global fashion, as prescribed by the theory of compressed sensing. Significant advantages follow, such as the fact that combining more data provides more information about the object of interest. Additionally, the influence of sparsity increases with the dimensionality.

Second, as explained by the authors themselves in their discussion [5], their reliance on an intermediate TV-inpainting step limits the capacity of their framework to reconstruct fines structures when only few pixels are scanned. The primary limitation is that performing TV-inpainting on strongly downsampled measurements tends to introduce important staircase artifacts in the restored images. In contrast, our approach is not limited by the morphology nor the fineness of the structures to be imaged. This translates into reconstruc-

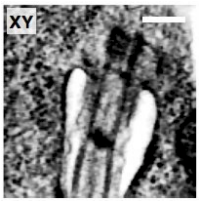

(a) Ground-truth

(b) Existing (50%)

(c) Proposed (50%)

(d) Existing (20%)

(e) Proposed (20%)

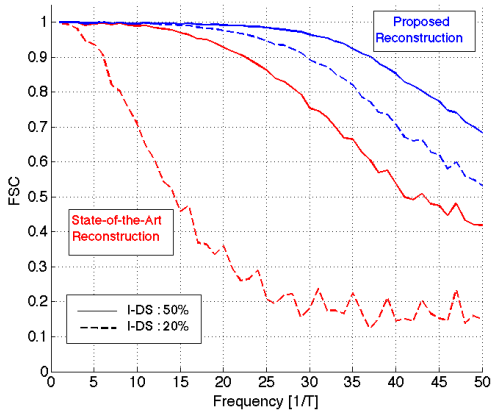

(f) FSC curves

Fig. 2. Comparison of the proposed algorithm with the existing algorithm for the reconstruction of synthetic random I-DS projection measurements of *T. brucei*. **(a)** xy-orthoview of the ground-truth volume. The scale bar indicates $500nm$. **(b)-(e)** Reconstructions achieved by the two algorithms from 50% and 20% randomly-downsampled RB-STEM measurements. **(f)** FSC curves of the reconstructed volumes for both algorithms at 50% and 20% downsampling. The spatial frequency at which the FSC curve falls below a certain FSC criterion (commonly fixed at FSC=0.5 in the community) indicates the achieved resolution.

tions of highly-detailed specimens that are globally more robust to the electron dosage reduction.

Finally, our approach also simplifies the optimization procedure as it only requires the optimization of a single hyper-parameter. The Matlab code implementing the proposed reconstruction algorithm is available online.[1]

5. CONCLUSION

The proposed regularized approach improves the tomographic reconstruction of heavily-downsampled RB-STEM measurements over the current state-of-the-art technique. This development opens new perspectives in the search for methods permitting lower-dose 3D STEM imaging of electron-sensitive samples without degrading the quality of the reconstructed volume Additional results on the proposed framework, *e.g.* an incoherence analysis of the RB-STEM acquisition scheme when the image is expressed in terms of wavelets, are the topic of a manuscript currently under review.

[1] http://bigwww.epfl.ch/algorithm/

6. REFERENCES

[1] S. J. Pennycook and P. D. Nellist, Eds., *Scanning Transmission Electron Microscopy*, Springer New York, New York, NY, 2011.

[2] M. F. Hohmann-Marriott, A. A. Sousa, A. A. Azari, S. Glushakova, G. Zhang, J. Zimmerberg, and R. D. Leapman, "Nanoscale 3D cellular imaging by axial scanning transmission electron tomography," *Nat. Methods*, vol. 6, no. 10, pp. 729–731, oct 2009.

[3] K. Aoyama, T. Takagi, A. Hirase, and A. Miyazawa, "STEM tomography for thick biological specimens," *Ultramicroscopy*, vol. 109, no. 1, pp. 70–80, 2008.

[4] A.E. Yakushevska, M.N. Lebbink, W.J.C. Geerts, L. Spek, E.G. van Donselaar, K.A. Jansen, B.M. Humbel, J.A. Post, A.J. Verkleij, and A.J. Koster, "STEM tomography in cell biology," *J. Struct. Biol.*, vol. 159, no. 3, pp. 381–391, 2007.

[5] Z. Saghi, M. Benning, R. Leary, M. Macias-Montero, A. Borras, and P. A. Midgley, "Reduced-dose and high-speed acquisition strategies for multi-dimensional electron microscopy," *Adv. Struct. Chem. Imaging*, vol. 1, no. 1, pp. 7, dec 2015.

[6] K. J. Batenburg, S. Bals., J. Sijbers, C. Kübel, P. A. Midgley, J. C. Hernandez, U. Kaiser, E. R. Encina, E. A.Coronado, and G. Van Tendeloo, "3D imaging of nanomaterials by discrete tomography," *Ultramicroscopy*, vol. 109, no. 6, pp. 730–740, 2009.

[7] S. Van Aert, K. J. Batenburg, M. D. Rossell, R. Erni, and G. Van Tendeloo, "Three-dimensional atomic imaging of crystalline nanoparticles," *Nature*, vol. 470, no. 7334, pp. 374–377, feb 2011.

[8] R. Leary, Z. Saghi, P. A. Midgley, and D. J. Holland, "Compressed sensing electron tomography," *Ultramicroscopy*, vol. 131, pp. 70–91, 2013.

[9] Z. Saghi, D. J. Holland, R. Leary, A. Falqui, G. Bertoni, A. J. Sederman, L. F. Gladden, and P. A. Midgley, "Three-Dimensional Morphology of Iron Oxide Nanoparticles with Reactive Concave Surfaces. A Compressed Sensing-Electron Tomography (CS-ET) Approach," *Nano Lett.*, vol. 11, no. 11, pp. 4666–4673, nov 2011.

[10] O. Nicoletti, F. de la Peña, R. K. Leary, D. J. Holland, C. Ducati, and P. A. Midgley, "Three-dimensional imaging of localized surface plasmon resonances of metal nanoparticles," *Nature*, vol. 502, no. 7469, pp. 80–84, oct 2013.

[11] B. Goris, S. Bals, W. Van den Broek, E. Carbó-Argibay, S. Gómez-Graña, L. M. Liz-Marzán, and G. Van Tendeloo, "Atomic-scale determination of surface facets in gold nanorods," *Nat. Mater.*, vol. 11, no. 11, pp. 930–935, oct 2012.

[12] J. P. Buban, Q. Ramasse, B. Gipson, N. D. Browning, and H. Stahlberg, "High-resolution low-dose scanning transmission electron microscopy.," *J. Electron Microsc. (Tokyo).*, vol. 59, no. 2, pp. 103–12, 2010.

[13] H. S. Anderson, J. Ilic-Helms, B. Rohrer, J. Wheeler, and K. Larson, "Sparse imaging for fast electron microscopy," *Proc. SPIE-IS&T Electron. Imaging*, vol. 8657, pp. 86570C, 2013.

[14] A. Stevens, H. Yang, L. Carin, I. Arslan, and N. D. Browning, "The potential for bayesian compressive sensing to significantly reduce electron dose in high-resolution STEM images," *Microscopy*, vol. 63, no. 1, pp. 41–51, 2014.

[15] E. J. Candes and M. B. Wakin, "An Introduction To Compressive Sampling," *IEEE Signal Process. Mag.*, vol. 25, no. 2, pp. 21–30, mar 2008.

[16] M. Nilchian, C. Vonesch, P. Modregger, M. Stampanoni, and M. Unser, "Fast iterative reconstruction of differential phase contrast X-ray tomograms," *Opt. Express*, vol. 21, no. 5, pp. 5511, mar 2013.

[17] M. Unser, "Sampling-50 years after Shannon," *Proc. IEEE*, vol. 88, no. 4, pp. 569–587, apr 2000.

[18] F. Natterer, *The Mathematics of Computerized Tomography*, Society for Industrial and Applied Mathematics, jan 2001.

[19] S. Ramani and J. A. Fessler, "A Splitting-Based Iterative Algorithm for Accelerated Statistical X-Ray CT Reconstruction," *IEEE Trans. Med. Imaging*, vol. 31, no. 3, pp. 677–688, mar 2012.

[20] S. Boyd, N. Parikh, E. Chu, B. Peleato, and J. Eckstein, "Distributed Optimization and Statistical Learning via the Alternating Direction Method of Multipliers," *Found. Trends® Mach. Learn.*, vol. 3, no. 1, pp. 1–122, 2010.

[21] M. Nilchian, J. P. Ward, C. Vonesch, and M. Unser, "Optimized kaiser-bessel window functions for computed tomography," *IEEE Transactions on Image Processing*, vol. 24, no. 11, pp. 3826–3833, Nov 2015.